

Article

# B<sub>4</sub>C Particles Reinforced Al2024 Composites via Mechanical Milling

Caleb Carreño-Gallardo <sup>1,\*</sup> , Ivanovich Estrada-Guel <sup>1</sup>, Claudia López-Meléndez <sup>2</sup>, Ernesto Ledezma-Sillas <sup>1</sup>, Rubén Castañeda-Balderas <sup>1</sup>, Raúl Pérez-Bustamante <sup>3</sup>  and José Martín Herrera-Ramírez <sup>1</sup>

<sup>1</sup> Advanced Materials Research Center (CIMAV), National Laboratory of Nanotechnology, Miguel de Cervantes No. 120, Chihuahua C.P. 31136, Mexico; ivanovich.estrada@cimav.edu.mx (I.E.-G.); jose.ledezma@cimav.edu.mx (E.L.-S.); ruben.castaneda@cimav.edu.mx (R.C.-B.); martin.herrera@cimav.edu.mx (J.M.H.-R.)

<sup>2</sup> La Salle University of Chihuahua, Prol. Lomas de Majalca No. 11201, Chihuahua C.P. 31020, Mexico; clopez@ulsachihuahua.edu.mx

<sup>3</sup> CONACYT-The Mexican Corporation for Research on Materials (COMIMSA), Ciencia y Tecnología 790, Fracc. Saltillo 400, Saltillo C.P. 25290, Mexico; rperezb@conacyt.mx

\* Correspondence: caleb.carreno@cimav.edu.mx; Tel.: +52-614-439-4816

Received: 13 July 2018; Accepted: 14 August 2018; Published: 17 August 2018



**Abstract:** The control of a homogeneous distribution of the reinforcing phase in aluminum matrix composites is the main issue during the synthesis of this kind of material. In this work, 2024 aluminum matrix composites reinforced with boron carbide were produced by mechanical milling, using 1 and 2 h of milling. After milling, powdered samples were cold consolidated, sintered and T6 heat treated. The morphology and microstructure of Al2024/B<sub>4</sub>C composites were investigated by scanning electron microscopy; analysis of X-ray diffraction peaks were used for the calculation of the crystallite size and microstrains by the Williamson–Hall method. The mechanical properties were evaluated by compression and hardness tests. B<sub>4</sub>C particles were found to be well dispersed into the aluminum matrix as a result of the high-energy milling process. The crystallite size of composites milled for 2 h was lower than those milled for 1 h. The hardness, yield strength and maximum strength were significantly improved in the composites processed for 2 h, in comparison to those processed for 1 h and the monolithic 2024 alloy.

**Keywords:** Al2024; boron carbide; mechanical milling

## 1. Introduction

Aluminum matrix composites are considered as promising materials for the development of the automotive and aerospace industry. This is because of the attractive characteristics, such as lightness, strength, high specific modulus and good corrosion resistance. For these reasons, extensive theoretical and experimental studies have been carried out on the fundamental relationships between the mechanical properties and the microstructure of metal matrix composites (MMCs) with different types of matrices and either particles or fibers as reinforcements [1–4]. The selection of the reinforcement type, geometry and volume fraction is critical for obtaining the best combination of properties with a low cost [5]. The size of the reinforcing phase is a key factor, in such a way that the interaction of particles with dislocations becomes of significant importance and, when they are considered with other strengthening effects typically found in conventional MMCs, gives as a result a remarkable improvement of the mechanical properties [6–9].

Another aspect to be considered in the synthesis of MMCs is the low wettability of ceramic particles with the molten metal matrix, which prohibits the production of MMCs by conventional

casting processes. Mechanical milling, a method of powder metallurgy, offers homogeneous dispersion of hard particles with a control of particle size. It also allows the fragmentation of ceramic clusters as well as the formation of alloys by diffusion mechanisms starting from pure metals, producing preforms by in situ reaction of reinforcements [10–14].

Monolithic  $B_4C$  ceramic is a low-density material having a high hardness, strength and stiffness. However, densification of monolithic  $B_4C$  requires the application of high temperatures and/or high pressures [15]. The density of  $B_4C$  is lower than that of other commercially available ceramic reinforcements, such as SiC,  $TiB_2$ ,  $ZrSiO_4$ ,  $Al_2O_3$ , and TiC, resulting in composites with higher specific stiffness. Due to the fact that it possesses a low density ( $2.52 \text{ g/cm}^3$ ), a hardness just below that of diamond ( $9.5 +$  in Mohs' scale), excellent thermal stability and wettability, remarkable chemical inertness, and high abrasive capacity, it is an ideal candidate as a reinforcement for aluminum-based composites [16]. However, a major limitation to its widespread use arises from its extreme susceptibility to brittle fracture. Researchers have known that combining  $B_4C$  with a metal could solve the recognized difficulties with  $B_4C$ . Therefore, this research focuses on the homogeneous dispersion of hard  $B_4C$  particles into the 2024 aircraft grade aluminum alloy. This is due to the extensive use of this alloy in structural applications and the potential for increasing its mechanical performance by adding hard particles. The use of solid-state routes, such as mechanical alloying to achieve an effective homogeneous dispersion of hard particles into different matrices, makes them an interesting way to be explored for expanding the mechanical capabilities of aluminum alloys, for future applications under room and hot working conditions. The evolution of the microstructure and mechanical properties of Al2024/ $B_4C$  composites prepared by mechanical milling and conventional sintering, followed by a T6 heat treatment, will be analyzed.

## 2. Materials and Methods

The raw materials used in this investigation were Al2024 alloy swarf, which was produced from a commercial solid bar, and  $B_4C$  particles of average diameter  $7 \mu\text{m}$  (Mills Electro Minerals Corp., Washington, DC, USA) were used as reinforcing agent. First of all, the Al2024 alloy swarf was mixed with  $B_4C$  in different concentrations (0.0, 0.5, 1.0, 1.5, 2.0, 2.5 wt.%) and then they were mechanically milled in a high-energy milling apparatus (SPEX 8000M, Metuchen, NJ, USA) for 1 and 2 h. AISI D2 vial and balls were selected as milling media. Milling process parameters were selected as follows: ball-to-powder ratio 5:1, argon atmosphere protection, and addition of methanol as a process control agent (PCA). After milling, the Al2024/ $B_4C$  composite mixtures were loaded into a steel die and uniaxially cold pressed using 900 MPa for 3 min to produce billets with a diameter of 6 mm and a height of 12 mm. Sintering process was carried out with a heating rate of  $15 \text{ }^\circ\text{C}/\text{min}$  up to  $500 \text{ }^\circ\text{C}$  for 3 h under an Ar atmosphere; samples were allowed to cool down inside the furnace. Finally, the samples were artificially aged (T6 temper) for 6 h at  $191 \text{ }^\circ\text{C}$  [17]. A monolithic Al2024 alloy was subjected to the same process for comparison purposes.

Microstructure, distribution and morphology of samples were determined using a scanning electron microscope (SEM, Hitachi SU3500, Tokyo, Japan). Crystallite size and microstrains were evaluated by X-ray diffraction (XRD) using  $\text{Cu K}\alpha$  ( $\lambda = 0.15406 \text{ nm}$ ) radiation source, in a diffractometer (BRUKER model D8 Advance, Billerica, MA, USA), in the  $2\theta$  range of  $20^\circ$ – $100^\circ$  operating at 40 kV/30 mA, with a scanning speed of  $0.005^\circ/\text{s}$ . Williamson–Hall analysis was used for estimating the crystallite size and microstrains, according to Equation (1). Metallographic specimens for the composites were prepared by cutting a cross section of samples followed by hot mounting. Sample were ground by using emery papers on a metallographic grinding machine. After that, a fine polish was made with high-alumina powder. Finally, samples were etched with Keller's reagent.

Vickers microhardness of the samples was measured at room temperature by a microhardness tester (FM-7, Tokyo, Japan) using a maximum load of 1 kgf and dwelling time of 15 s; a total of five measurements were performed for each sample, and the average value was reported. Compression tests were performed at room temperature in a universal testing machine (Instron, Norwood, MA,

USA) with a constant cross-head speed of 0.5 mm/min to obtain the yield strength ( $\sigma_y$ ) and maximum strength ( $\sigma_{max}$ ); three measurements were achieved for each sample and the average value was reported. Additionally, the fracture surfaces were further examined in detail by SEM.

$$\beta \cos(\theta) = \frac{K\lambda}{D} + 4\epsilon \sin \theta \quad (1)$$

where:  $\beta$  = FWHM,  $D$  = crystallite size,  $\epsilon$  = strain,  $\lambda$  = wavelength of Cu  $K_{\alpha}$ , and  $K$  = shape factor (0.9).

### 3. Results and Discussion

#### 3.1. Microstructure Analysis

Figure 1 shows images of the Al2024 alloy swarf and the as-received  $B_4C$  powder, the latter presenting a wide distribution of particle size with an angular morphology. Figure 2 shows the milling effect on the morphology and particle size of the Al2024-2.0 wt.%  $B_4C$  composite. After 1 h of milling (Figure 2a), the particles have an equiaxial morphology and wide particle size distribution. When the milling time increases to 2 h (Figure 2b), the micro-scale particles present a noticeable refinement. The increment in milling time produces hardened particles due to cold working [18] owing to the predominance of the fracture stage in the fracture-welding process occurring during the mechanical milling.

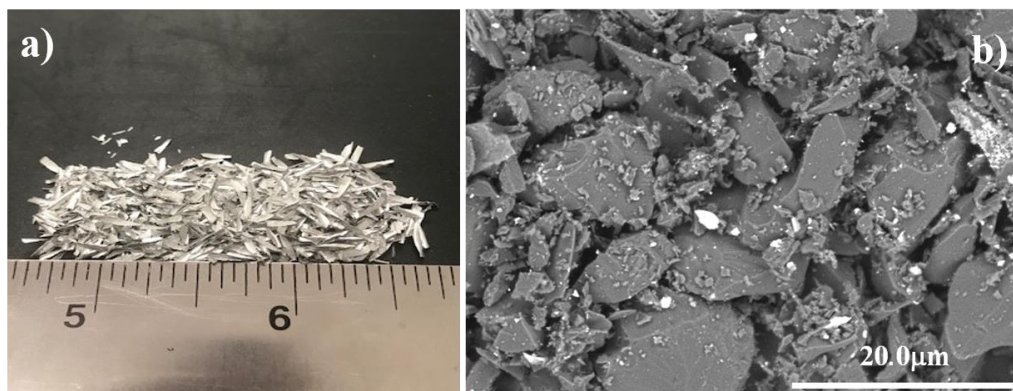


**Figure 1.** (a) Photography of the Al2024 alloy swarf and (b) Backscattered electron-scanning electron microscope (BE-SEM) image of the  $B_4C$  powder.

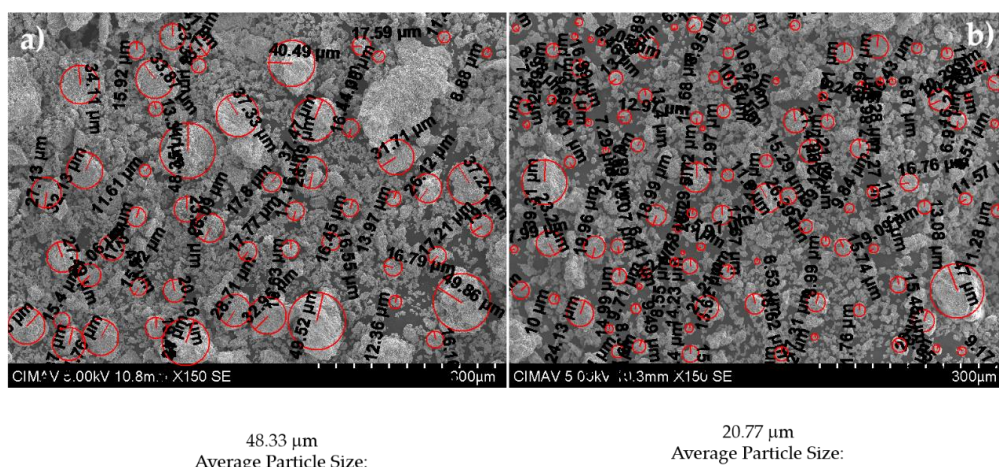


**Figure 2.** Secondary electron-scanning electron microscope (SE-SEM) micrographs of the Al2024-2.0 wt.%  $B_4C$  composite milled during (a) 1 h and (b) 2 h.

Figure 3 shows XRD diffraction patterns of the as-milled Al2024 alloy (0.0 wt.% B<sub>4</sub>C) and its composites as a function of the B<sub>4</sub>C concentration. A respective inset displays the effect of milling time and B<sub>4</sub>C concentration on the macrostrains and crystallite size. No significant decrease in the intensity of the X-ray diffraction peaks nor broadening are visible in the patterns. However, a deeper analysis indicates changes in the crystallite size and variations in the microstrains as the milling time increases from 1 to 2 h, and as a function of the B<sub>4</sub>C concentration. A decrement in crystallite size is observed when milling time increases from 1 to 2 h. This effect can be attributed to the increment in the milling time producing a size reduction of the B<sub>4</sub>C particles.

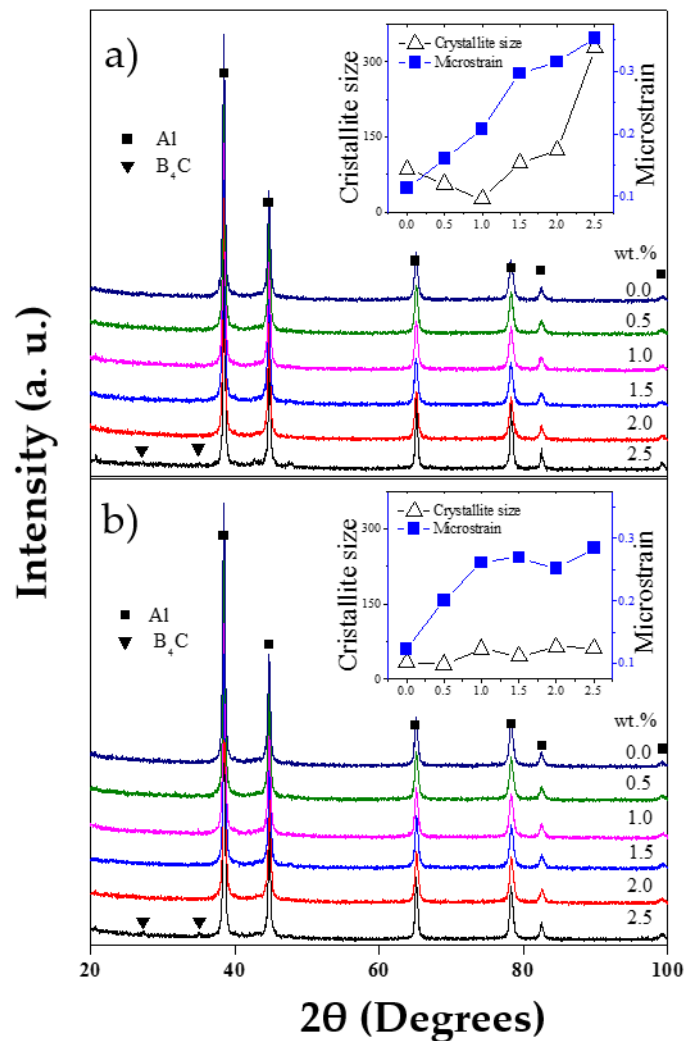


**Figure 3.** X-ray diffraction (XRD) diffraction patterns, crystallite size and microstrains as a function of the B<sub>4</sub>C content: (a) 1 h and (b) 2 h of milling.

When the as-milled powders were sintered and T6 heat treated, the reinforcing particles became smaller and sub-rounded (Figure 4a); furthermore, the particles can be seen as well embedded and homogeneously distributed throughout the Al2024 matrix, with no areas substantially depleted of B<sub>4</sub>C (Figure 4b). The spacing between the B<sub>4</sub>C particles varies from 0 to 20 μm, with an average of about 8 μm. At higher magnifications (Figure 4b,c), it is noticeable that the B<sub>4</sub>C particles have different sizes ranging from 3 to 20 μm. The properties of the MMCs depend not only on the matrix, particle morphology and the volume fraction, but also on the distribution of the reinforcing particles, as well as the interface bonding between the particle and the matrix [19,20]; a good interface bonding can be

seen in the representative image shown in Figure 4c. The most important factor in the fabrication of MMCs is the uniform dispersion of the reinforcing phase.

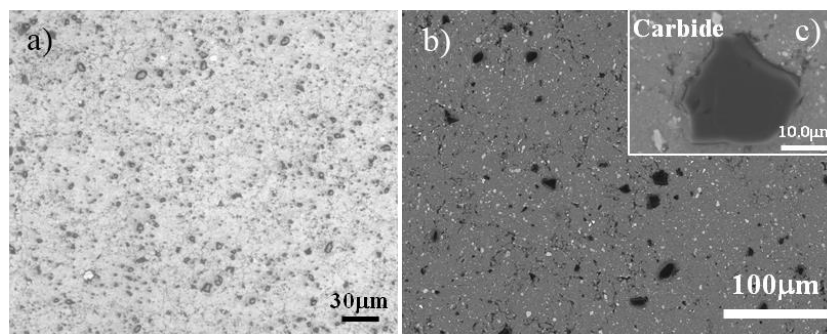


**Figure 4.** Al2024-2.0 wt.% B<sub>4</sub>C specimen milled for 2 h, sintered and T6 heat treated: (a) low-magnification optical micrograph and (b) high-magnification SEM micrograph; (c) morphology of a single B<sub>4</sub>C particle.

The spatial distribution of the elements in the composites after the T6 heat treatment was examined through a scanning electron microscope with energy dispersive spectroscopy (SEM-EDS) mapping, as shown in Figure 5a for the Al2024-2.0 wt.% B<sub>4</sub>C specimen. The mapping reveals a homogeneous distribution of the B<sub>4</sub>C particles, even though they present a varied particle size. The energy dispersive spectroscopy (EDS) analysis taken from one of the bigger particles (Figure 5b) confirmed the chemical composition of the B<sub>4</sub>C phase.

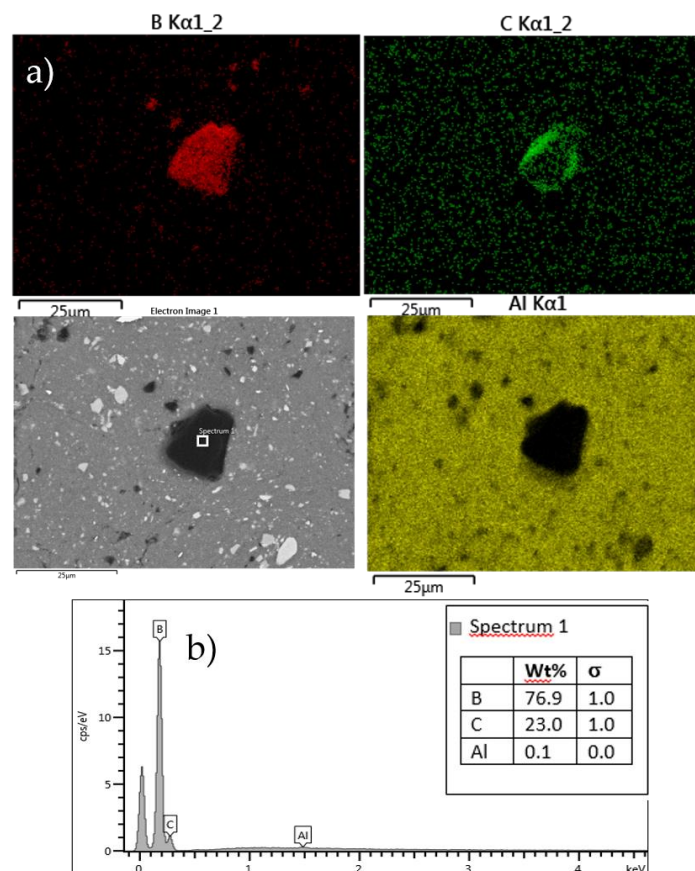


**Figure 5.** (a) scanning electron microscope-energy dispersive spectroscopy (SEM-EDS) mapping analysis of the Al2024-2.0 wt.% B<sub>4</sub>C milled for 2 h; (b) EDS analysis of a B<sub>4</sub>C particle.

### 3.2. Mechanical Properties

#### 3.2.1. Microhardness Measurements

The microhardness results of the composites milled for 1 and 2 h are shown in Figure 6; the error bars represent the standard deviation. As can be seen, the microhardness of the composites increases with the increment in the milling time, which is related to the material strain hardening during the mechanical process. On the other hand, for both milling conditions, the microhardness of the composites increases with increments in the  $B_4C$  content up to 2.0 wt.%, reaching values of 110 and 125 HV for samples milled for 1 and 2 h, respectively. These values represent an increment in microhardness of around 45% and 68%, respectively, compared with the microhardness of a commercial as-cast 2024 aluminum alloy with T6 heat treatment condition (76 HV) [21]. These increments in microhardness are associated with the combined effects of the homogeneous distribution of the  $B_4C$  particles into the Al2024 matrix and the overall microstructure refinement induced by the milling process. From 2.5 wt.% of  $B_4C$ , the microhardness begins to decrease, which may be due to the carbon matrix saturation [22].

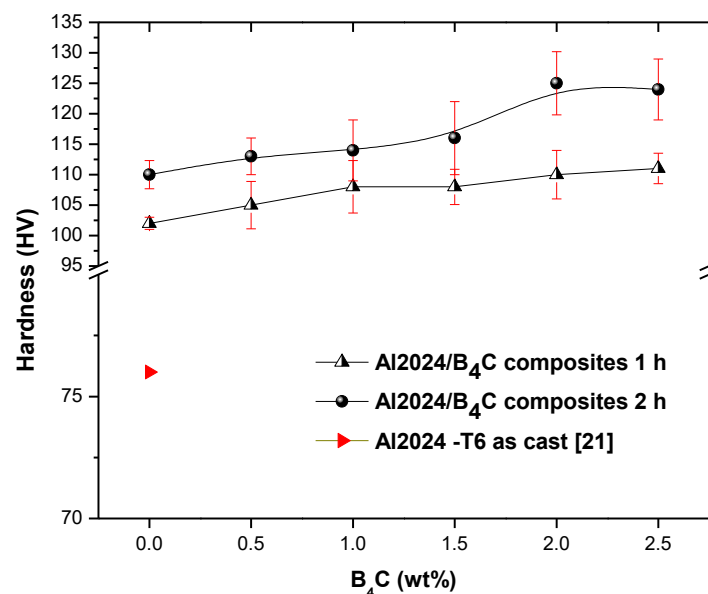


**Figure 6.** Effect of the  $B_4C$  content and milling time on the microhardness of the Al2024/ $B_4C$  composites.

#### 3.2.2. Compression Tests

Figure 7 presents the effect of the  $B_4C$  addition and milling time on the yield strength ( $\sigma_y$ ) of the composites; the error bars represent the standard deviation. Similar to the hardness results, there is a clear influence of the  $B_4C$  content on the  $\sigma_y$  behavior, up to saturation values of about 338 and 440 MPa for samples milled for 1 and 2 h, respectively. With 2.5 wt.% of  $B_4C$  the  $\sigma_y$  of composites begins to decrease. Concerning the milling time effect, it is evident how  $\sigma_y$  increases for all composites milled for 2 h, in comparison with those milled for 1 h. Figure 7 shows also the  $\sigma_y$  value reported in the literature for the as-cast Al2024 alloy in the T6 heat treated condition (315 MPa) [21]. Samples milled for 1 h containing between 1.5 and 2.0 wt.% of  $B_4C$  exceed the  $\sigma_y$  value of the commercial sample. The low  $\sigma_y$  values of samples milled for 1 h with 0.5 and 1.0 wt.% of  $B_4C$  can be due to the porosity inherent to the sintering process [23]. All composites milled for 2 h exceeded the  $\sigma_y$  value of the commercial sample, which proves the positive effect of the mechanical milling process in counteracting the adverse effect of the porosity in the sintered samples. In the case of the sample milled for 2 h with 1.5 wt.% of  $B_4C$ , the positive trend was broken. For both milling times, with 2.5 wt.% of  $B_4C$  the  $\sigma_y$  begins to

decrease, probably because of the matrix saturation, but still these values are higher than that of the commercial sample.

Regarding the maximum strength ( $\sigma_{\max}$ ), whose values are shown in Figure 8, the effect of the  $B_4C$  content and the milling time were comparable to those found for the yield strength. Similar to other research works [24–27], the strengthening mechanisms involved here can be related to the following: (i) the dispersion of second phases ( $B_4C$  particles); (ii) the microstructure refinement induced by the high-energy milling; and (iii) the grain-boundary strengthening (Hall-Petch effect). Even though the Orowan strengthening mechanism does not occur in composites with microreinforcements, the particle fragmentation due to milling effects must be considered, and thus this mechanism may be considered owing to the presence of fragmented  $B_4C$  particles finely dispersed into the Al2024 alloy matrix.

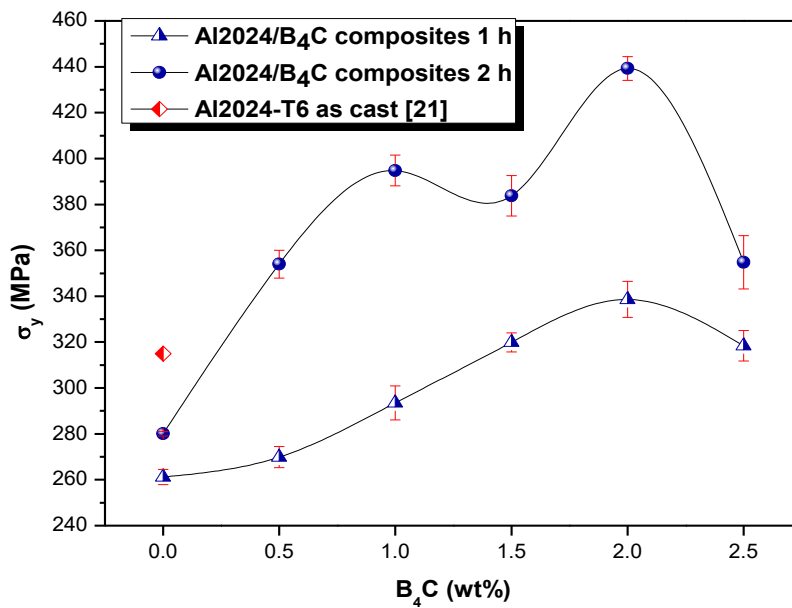


Figure 7. Yield strength ( $\sigma_y$ ) as a function of the  $B_4C$  content and milling time.

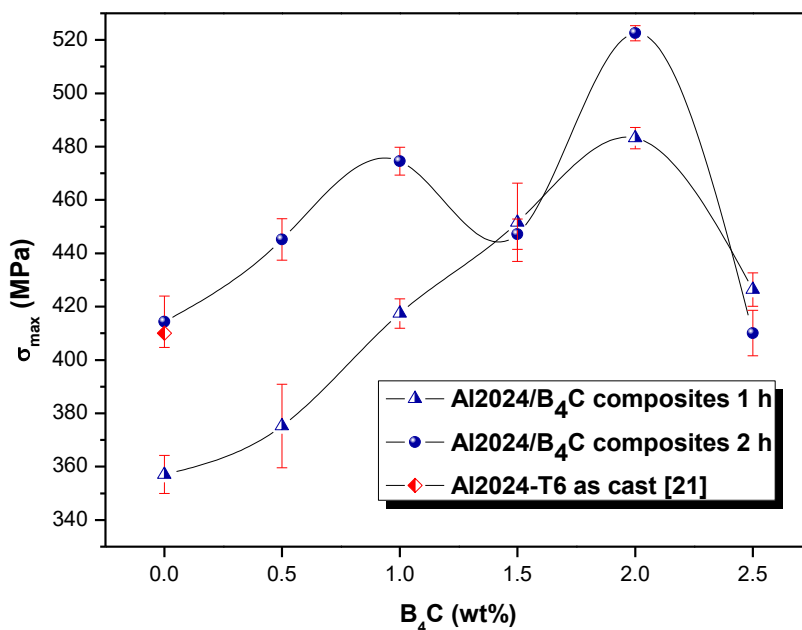
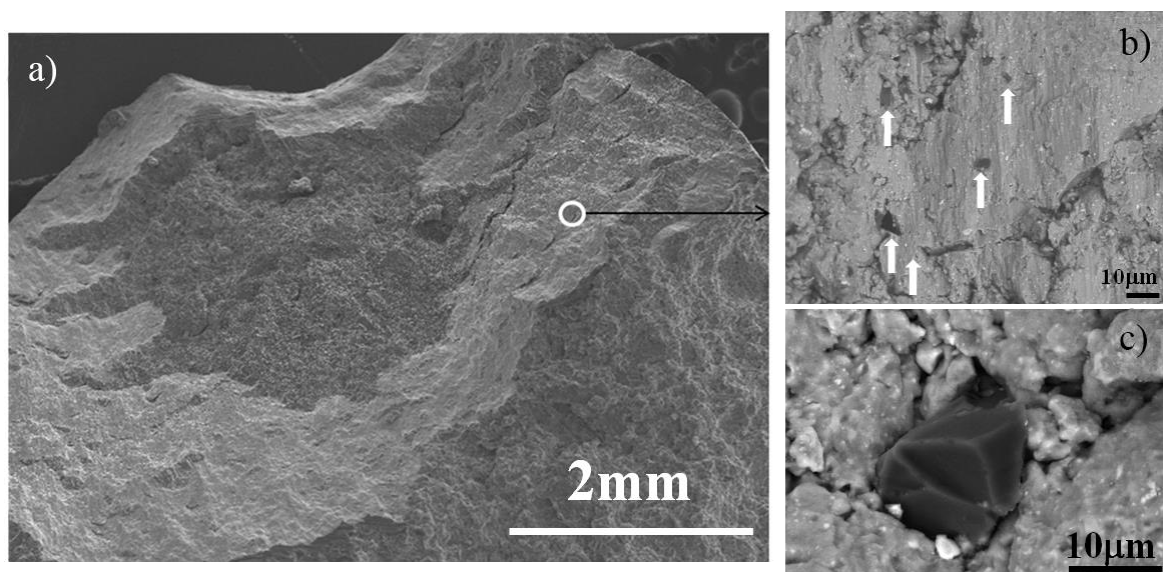


Figure 8. Maximum strength ( $\sigma_{\max}$ ) as a function of the  $B_4C$  content and milling time.

### 3.3. Fractographic analysis

Figure 9a shows the fracture surface of the Al2024-2.0 wt.% B<sub>4</sub>C composite milled for 2 h. Intact B<sub>4</sub>C particles can be observed on the surface of fractured samples (pointed by arrows in Figure 9b), which indicates a good bonding between B<sub>4</sub>C particles and the Al2024 alloy matrix. Axial cracks similar to those presented in brittle materials under uniaxial loads during compression tests can be observed. In addition, it can be seen that the sample was broken along the loading direction. This suggests that the addition of 2.0 wt.% of B<sub>4</sub>C improves the ductility of the composite material; however, this behavior must be deeply analyzed in future work. Some fracture dimples around the B<sub>4</sub>C particles were found (Figure 9c), which were formed at the microscopic level by the mechanism of ductile failure of the Al2024 matrix. A full examination of the fracture surface of samples demonstrated the scarcity of cracking in the reinforcement; a decohesion of the matrix/reinforcement interface could not be seen either. These results indicate the formation of a strong interface allowing the load to be efficiently transferred between the matrix and the reinforcing particles.



**Figure 9.** (a) Fracture surface examination of the Al2024-2.0 wt.% B<sub>4</sub>C composite milled for 2 h; (b) B<sub>4</sub>C particles on the fractured surface and (c) Fracture dimples around the B<sub>4</sub>C particles.

## 4. Conclusions

The milling process, followed by cold compaction, sintering and T6 heat treatment, were successfully applied to reinforce the 2024 aluminum alloy with B<sub>4</sub>C. B<sub>4</sub>C particles were homogeneously dispersed throughout the 2024 aluminum matrix. A strong interface bonding between B<sub>4</sub>C and Al2024 was achieved with no reaction between them during the whole synthesis process. The milling time had an effect on the refinement of the crystallite size and microstrains increase for both milling times (1 and 2 h). An increase in the amount of B<sub>4</sub>C in the Al2024 matrix did not result in a finer crystallite size for all composites milled for 2 h; however, for composites milled for 1 h, the amount of reinforcement increased both the crystallite size and microstrains. Defects such as pores and cracks were not detected. Both milling time and B<sub>4</sub>C content had a positive effect on the mechanical properties of the composites. The best properties, hardness,  $\sigma_y$ , and  $\sigma_{max}$ , were obtained with 2 h of milling and 2.0 wt.% of B<sub>4</sub>C particles.

**Author Contributions:** C.L.-M. and E.L.-S. prepared metallographic samples; R.C.-B. developed the composites by mechanical milling; R.P.-B. and J.M.H.-R. characterized the composite powders by SEM; I.E.-G. characterized the samples by microhardness and compression tests; C.C.-G. designed the experiments, analyzed the data and wrote the paper.

**Acknowledgments:** The authors thank to Red Tematica de Nanociencias y Nanotecnologia, Red Tematica Nacional de Aeronautica and Red Tematica de Materiales Compuestos. The authors gratefully acknowledge the efforts of D. Lardizabal-Gutierrez and K. Campos-Venegas for their technical assistance.

**Conflicts of Interest:** The authors declare no conflict of interest.

## References

1. Zheng, R.X.; Hao, X.; Yuan, Y.; Ma, C. Effect of high volume fraction of B<sub>4</sub>C particles on the microstructure and mechanical properties of aluminum alloy based composites. *J. Alloy. Compd.* **2013**, *576*, 291–298. [[CrossRef](#)]
2. Ganesh, V.V.; Chawla, N. Effect of particle orientation anisotropy on the tensile behavior of metal matrix composites: Experiments and microstructure-based simulation. *Mater. Sci. Eng. A* **2005**, *391*, 342–353. [[CrossRef](#)]
3. Bethune, D.S.; Bethune, D.S.; Kiang, C.H.; De Vries, M.S.; Gorman, G.; Savoy, R.; Vazquez, J.; Beyers, R. Cobalt-catalysed growth of carbon nanotubes with single-atomic-layer walls. *Nature* **1993**, *363*, 605–607. [[CrossRef](#)]
4. Friler, J.B.; Argon, A.S.; Cornie, J.A. Strength and toughness of carbon fiber reinforced aluminum matrix composites. *Mater. Sci. Eng. A* **1993**, *162*, 143–152. [[CrossRef](#)]
5. Davies, C.H.J.; Raghunathan, N.; Sheppard, T. Structure–property relationships of SiC reinforced advanced Al–Zn–Mg–Cu alloy. *Mater. Sci. Technol.* **1992**, *8*, 977–984. [[CrossRef](#)]
6. Zhang, Z.; Chen, D.L. Contribution of Orowan strengthening effect in particulate-reinforced metal matrix nanocomposites. *Mater. Sci. Eng. A* **2008**, *483*, 148–152. [[CrossRef](#)]
7. Zhang, Z.; Chen, D.L. Consideration of orowan strengthening effect in particulate-reinforced metal matrix nanocomposites: A model for predicting their yield strength. *Scr. Mater.* **2006**, *54*, 1321–1326. [[CrossRef](#)]
8. Sanaty-Zadeh, A. Comparison between current models for the strength of particulate-reinforced metal matrix nanocomposites with emphasis on consideration of hall–petch effect. *Mater. Sci. Eng. A* **2012**, *531*, 112–118. [[CrossRef](#)]
9. Luo, P.; McDonald, D.T.; Xu, W.; Palanisamy, S.; Dargusch, M.S.; Xia, K. A modified hall–petch relationship in ultrafine-grained titanium recycled from chips by equal channel angular pressing. *Scr. Mater.* **2012**, *66*, 785–788. [[CrossRef](#)]
10. Shehata, F.; Fathy, A.; Abdelhameed, M.; Moustafa, S.F. Preparation and properties of Al<sub>2</sub>O<sub>3</sub> nanoparticle reinforced copper matrix composites by in situ processing. *Mater. Des.* **2009**, *30*, 2756–2762. [[CrossRef](#)]
11. Carreño-Gallardo, C.; Estrada-Guel, I.; Romero-Romo, M.; Cruz-García, R.; López-Meléndez, C.; Martínez-Sánchez, R. Characterization of Al<sub>2</sub>O<sub>3</sub>NP–Al2024 and AgCNP–Al2024 composites prepared by mechanical processing in a high energy ball mill. *J. Alloy. Compd.* **2012**, *536*, 26–30. [[CrossRef](#)]
12. Kollo, L.; Leparoux, M.; Bradbury, C.R.; Jäggi, C.; Carreño-Morelli, E.; Rodríguez-Arbaizar, M. Investigation of planetary milling for nano-silicon carbide reinforced aluminium metal matrix composites. *J. Alloy. Compd.* **2010**, *489*, 394–400. [[CrossRef](#)]
13. De Cicco, M.; Turng, L.S.; Li, X.C.; Perepezko, J.H. Production of semi-solid slurry through heterogeneous nucleation in metal matrix nanocomposites (MMNC) using nano-scale ultrasonically dispersed inoculants. *Solid State Phenom.* **2008**, *141–143*, 487–492.
14. Lai, M.O.; Lu, L.; Laing, W. Formation of magnesium nanocomposite via mechanical milling. *Compos. Struct.* **2004**, *66*, 301–304. [[CrossRef](#)]
15. Thévenot, F. Boron carbide—A comprehensive review. *J. Eur. Ceram. Soc.* **1990**, *6*, 205–225. [[CrossRef](#)]
16. Wu, C.; Shen, Q.; Luo, G.; Fang, P.; Li, C.; Wang, Y.; Zhang, L. Microstructure and mechanical properties of Al-7075/B<sub>4</sub>C composites fabricated by plasma activated sintering. *J. Alloy. Compd.* **2014**, *588*, 265–270.
17. Bray, G.H.; Glazov, M.; Rioja, R.J.; Li, D.; Gangloff, R.P. Effect of artificial aging on the fatigue crack propagation resistance of 2000 series aluminum alloys. *Int. J. Fatigue* **2001**, *23*, 265–276. [[CrossRef](#)]
18. Suryanarayana, C. Mechanical alloying and milling. *Prog. Mater. Sci.* **2001**, *1–2*, 1–184. [[CrossRef](#)]
19. Sahin, Y. Preparation and some properties of SiC particle reinforced aluminium alloy composites. *Mater. Des.* **2003**, *24*, 671–679. [[CrossRef](#)]

20. Saboori, A.; Moheimani, S.K.; Dadkhah, M.; Pavese, M.; Badini, C.; Fino, P. An overview of key challenges in the fabrication of metal matrix nanocomposites reinforced by graphene nanoplatelets. *Metals* **2018**, *8*, 172. [[CrossRef](#)]
21. Matweb, Material Property Data. Available online: <http://www.matweb.com>. (accessed on 15 April 2018).
22. Pérez-Bustamante, R.; Pérez-Bustamante, F.; Maldonado-Orozco, M.C.; Martínez-Sánchez, R. The effect of heat treatment on microstructure evolution in artificially aged carbon nanotube/Al2024 composites synthesized by mechanical alloying. *Mater. Charact.* **2017**, *126*, 28–34. [[CrossRef](#)]
23. Xue, L.; Wierzbicki, T. Ductile fracture characterization of aluminum alloy 2024-T351 using damage plasticity theory. *Int. J. Appl. Mech.* **2009**, *1*, 267–304. [[CrossRef](#)]
24. Angers, R.; Krishnadev, M.R.; Tremblay, R.; Corriveau, J.-F.; Dubé, D. Characterization of SiC<sub>p</sub>/2024 aluminum alloy composites prepared by mechanical processing in a low energy ball mill. *Mater. Sci. Eng. A* **1999**, *262*, 9–15. [[CrossRef](#)]
25. Vaidya, R.U.; Song, S.G.; Zurek, A.K. Dynamic mechanical response and thermal expansion of ceramic particle reinforced aluminium 6061 matrix composites. *Philos. Mag. A* **1994**, *70*, 819–836. [[CrossRef](#)]
26. Yang, Y.; Lan, J.; Li, X. Study on bulk aluminum matrix nano-composite fabricated by ultrasonic dispersion of nano-sized SiC particles in molten aluminum alloy. *Mater. Sci. Eng. A* **2004**, *380*, 378–383. [[CrossRef](#)]
27. Martínez-Sánchez, R.; Reyes-Gasga, J.; Caudillo, R.; García-Gutierrez, D.I.; Márquez-Lucero, A.; Estrada-Guel, I.; Mendoza-Ruiz, D.C.; José-Yacaman, M. Mechanical and microstructural characterization of aluminum reinforced with carbon-coated silver nanoparticles. *J. Alloy. Compd.* **2007**, *438*, 195–201. [[CrossRef](#)]



© 2018 by the authors. Licensee MDPI, Basel, Switzerland. This article is an open access article distributed under the terms and conditions of the Creative Commons Attribution (CC BY) license (<http://creativecommons.org/licenses/by/4.0/>).